Nanoscale
Advances

ROYAL SOCIETY
OF CHEMISTRY

PAPER
Leanne D. Chen *et al.*
A density functional theory investigation of ammonia
oxidation pathways on nickel oxide

NCNST

PAPER

Check for updates

A density functional theory investigation of ammonia oxidation pathways on nickel oxide†

Brendan D. Paget, [ID] Shayne J. Johnston, Henry Lim and Leanne D. Chen [ID] *

Direct ammonia fuel cells (DAFCs) utilize ammonia's chemical energy and convert it into electricity through the electrocatalyzed ammonia oxidation reaction (AOR). To date, studies have focused on Pt-based anode materials; however due to limitations, research has shifted towards alternative materials. Previous research in our group has focused on oxidized Ni-based materials including $Ni(OH)_2$ and $NiOOH$ which show promising catalytic activity. The current study used density functional theory to determine the catalytic activity of NiO. It was found that the potential determining step for all mechanisms associated with AOR is the first deprotonation from $*NH_3$ to $*NH_2$, requiring 1.25 eV. Additionally, the lattice oxygens on the surface provide alternate mechanistic routes compared to the previously studied $Ni(OH)_2$ and $NiOOH$. This work outlines the ability of NiO to drive various mechanisms toward $N_2(g)$, $N_2H_4(g)$, $NO(g)$, $NO_2^-(aq)$, $NO_3^-(aq)$, and $N_2O(g)$.

1 Introduction

Fossil fuels are commonly used to generate power and energy around the world. Common fuel sources such as coal, oil and natural-gas currently power industrial growth and advance the development of society.[1–3] However, the use of these resources raises significant environmental concerns, contributing to air and water pollution, climate change, and global warming.[2] In recent years, these concerns have increased to alarming levels, which has initiated an effort to transition our energy production away from using fossil fuels to alternative technologies such as solar, wind and other renewable energy sources.[4] The currently established renewable energy sources significantly reduce the amount of greenhouse gas emissions that are emitted into our atmosphere. Although this is a promising step forward in the effort to reduce the usage of fossil fuels, these technologies are not yet capable of meeting global energy demand.[5] As society continues to rely on fossil fuels, there is a demand to find an alternative solution for energy production. This solution needs to provide a clean and scalable source of energy, capable of producing enough energy to transition towards a low-carbon future. A solution for this transition towards a low-carbon future is the adoption of the hydrogen economy, where hydrogen gas (H_2) is used as the primary fuel and energy source.[6,7] Hydrogen can generate energy through combustion into water and heat,[8] or through electrochemical conversion as seen in fuel cells.[7,9,10] Hydrogen, however, has notable limitations that significantly restrict its adoption as

a primary energy carrier. Some of these challenges involve storage and transportation, limiting hydrogen's large-scale implementation into a wide range of technologies.[11] Ammonia (NH_3) has emerged as a promising alternative fuel source within the hydrogen economy. Due to ammonia's high hydrogen content (17.6 wt%), it can serve as a valuable energy and hydrogen carrier.[12] In comparison to hydrogen gas, ammonia is easier to store and transport as it can be stored as a liquid at 20 °C with an applied pressure of 8.6 bar, rendering it a more practical option as a fuel source.[13] Furthermore, one of the main contributors to ammonia being a valuable alternative is that it can act as both a direct and indirect fuel source, allowing it to be used across a range of technologies that are being developed and currently exist. Among these, direct ammonia fuel cells (DAFCs) have gained attention as an efficient technology to convert ammonia's stored chemical energy into electricity.[11]

1.1 Direct ammonia fuel cells

Direct ammonia fuel cells (DAFCs) have seen an increase in scientific studies over the past few years as fuel cell research transitions to finding alternative fuel sources beyond conventional hydrogen gas. As recent findings on ammonia's fuel source capability emerge, anode material development has become an area of focus to further optimize DAFCs. DAFCs work by converting ammonia's chemical energy into electricity through the electrochemical oxidation reaction at the anode.[14] This reaction in DAFCs ultimately forms nitrogen gas (N_2), protons (H^+), and electrons by proceeding through the mechanisms shown in Fig. 1. These protons migrate through the electrolyte towards the cathode where they combine with oxygen and electrons to produce H_2O. Under basic conditions (pH = 14), the AOR is commonly written as:

Electrochemical Technology Centre, Department of Chemistry, University of Guelph, Guelph, Ontario N1G 2W1, Canada. E-mail: leanne.chen@uoguelph.ca
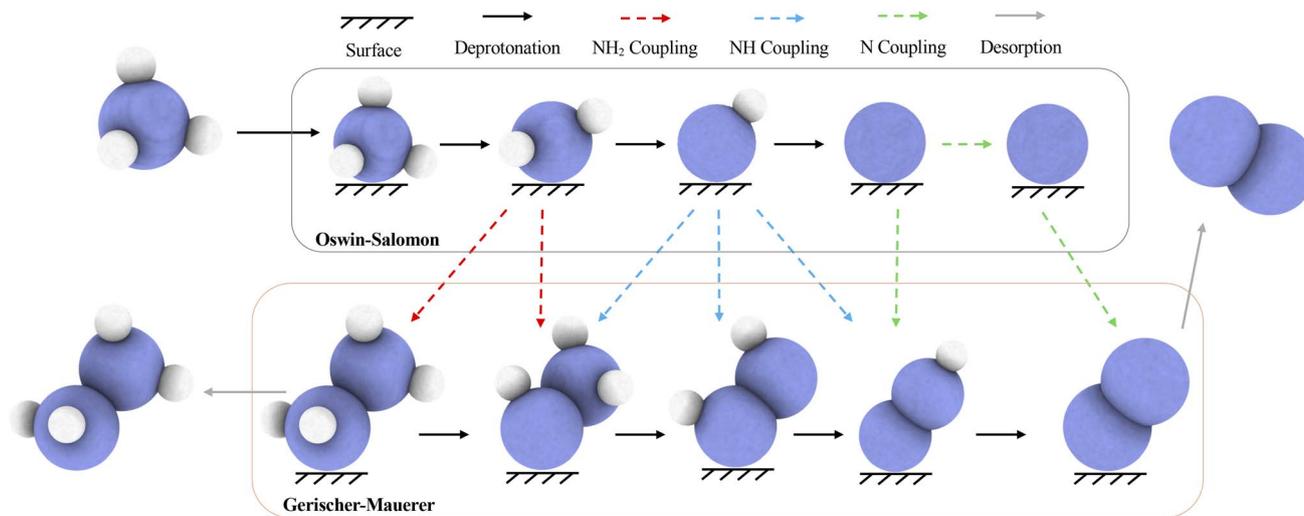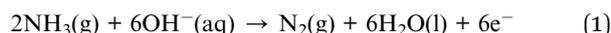
Fig. 1 AOR mechanisms toward N_2 and N_2H_4 formation. Blue and white spheres are nitrogen and hydrogen atoms, respectively. The Oswin–Salomon mechanism and the Gerischer–Mauerer mechanism are outlined by a black and orange box, respectively.

$$2NH_3(g) + 6OH^-(aq) \rightarrow N_2(g) + 6H_2O(l) + 6e^- \quad (1)$$

By convention, all redox reactions are written as reductions to allow for direct comparison in the electrochemical series.[15] Thus, all reactions associated with the AOR will be written as the reverse reaction, known as the nitrogen reduction reaction (NRR), as shown in eqn (2). This work will report reduction potentials consistent with the electrochemical series convention to avoid any confusion about the thermodynamics of a given reaction.

$$N_2(g) + 6H^+(aq) + 6e^- \rightarrow 2NH_3(g) \quad U° = +0.0567 \text{ V}_{RHE} \quad (2)$$

Electrode reactions referenced to the reversible hydrogen electrode (RHE) are pH-invariant, while those references to the standard hydrogen electrode (SHE) depend on pH. Since the AOR occurs under alkaline conditions, the standard electrode potential for the AOR takes on a different value at pH 14:

$$N_2(g) + 6H_2O(l) + 6e^- \rightarrow$$
$$2NH_3(g) + 6OH^-(aq) \quad U° = -0.772 \text{ V}_{SHE, pH = 14} \quad (3)$$
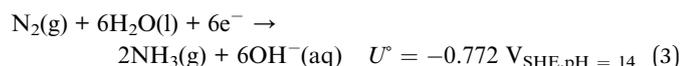
1.2 Anode materials

Various studies have focused on the development and analysis of anode materials which catalyze the ammonia oxidation reaction. In a study by De Vooys *et al.*, the AOR was investigated on transition metals such as platinum (Pt), palladium (Pd), iridium (Ir), rhodium (Rh) and ruthenium (Ru).[16] This study outlined the ability of Pt to catalyze the AOR and identified it as the most active catalyst.[16] In another study, it was shown that the combination of Pt with Ir to form a bi-metallic catalyst improved the performance of the anode.[17] Multiple mechanistic studies[18–22] have been carried out on Pt-based catalysts due to the metal's catalytic ability to deprotonate AOR intermediates.[16]

Pt-based materials have shown that the main product is $N_2(g)$[23] and are commonly used as a benchmark when comparing AOR catalysts due to their high AOR peak current and low onset potentials.[16,24–27] Despite their catalytic ability, Pt-based catalysts present notable challenges. Short lifetimes, and electrode deactivation due to intermediate poisoning hinder their broad adoption into real-world applications. Depending on the applied potential, the Pt surface can be poisoned by *N or *NO.[18,28] Due to these limitations, there is interest in developing electro-catalytic surfaces, using less expensive metals that are capable of avoiding poisoning and maintaining activity.

Previous experimental studies have investigated the AOR on $Ni(OH)_2$/NiOOH-based catalysts.[29,30] It has been shown that using Ni-based catalysts for AOR can improve the activity and overall lifetime of the electrocatalyst.[29–31] Furthermore, these Ni-based materials are promising as they are resistant to poisoning and low-cost, and produce dinitrogen, nitrite, and nitrate,[29,30] each of which will be discussed in the context of their formation mechanisms in the following sections. Through understanding of the AOR mechanism, key reaction intermediates and potential determining steps can be identified.
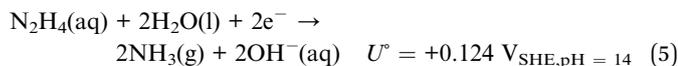
1.3 AOR mechanism

Two primary mechanisms for the formation of $N_2(g)$ have been proposed: the Oswin–Salomon (O–S) mechanism, and the Gerischer–Mauerer (G–M) mechanism. In the O–S pathway, ammonia undergoes subsequent deprotonation steps to form atomic nitrogen, which then recombines to form $N_2(g)$.[37] More recently discovered, the G–M mechanism involves the partially dehydrogenated intermediates, NH_x (where x can be 0, 1, or 2), reacting with each other to form coupled intermediates such as hydrazine (N_2H_4) prior to further deprotonation towards $N_2(g)$.[38] The G–M mechanism is supported through the formation of N_2H_4 as a detectable intermediate, which is seen as a two-electron reduction to form ammonia, as shown in eqn (4) and (5):

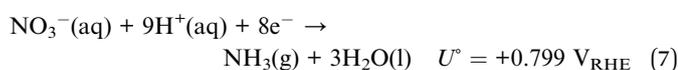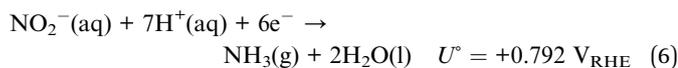$$N_2H_4(aq) + 2H^+(aq) + 2e^- \rightarrow$$
$$2NH_3(g) \quad U^\circ = +0.867 \; V_{RHE} \quad (4)$$
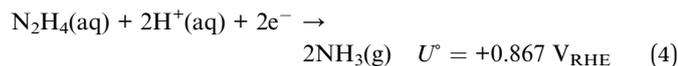
And compared on the SHE scale under alkaline conditions:

$$N_2H_4(aq) + 2H_2O(l) + 2e^- \rightarrow$$
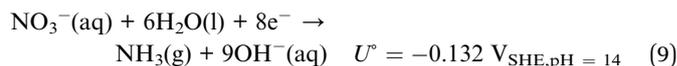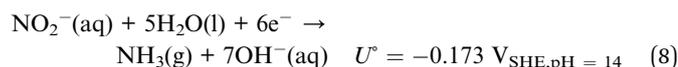$$2NH_3(g) + 2OH^-(aq) \quad U^\circ = +0.124 \; V_{SHE,pH\,=\,14} \quad (5)$$

Both of these mechanisms were originally proposed using platinum black electrodes, but they differ in the intermediate species that were involved.[37,38] The pathways can be seen in Fig. 1.
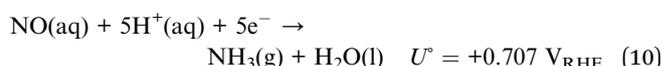
1.4 Further oxidation

Beyond the formation of dinitrogen, other studies have suggested the possibility of different oxidation reactions towards the formation of nitrite, $NO_2^-(aq)$ and nitrate, $NO_3^-(aq)$.[28] The respective reduction reactions for these products can be seen in eqn (6) and (7), compared using the RHE scale, and in eqn (8) and (9), when compared to SHE under alkaline conditions where pH = 14.
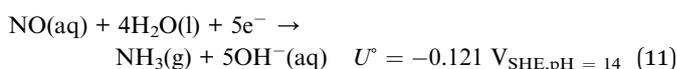
$$NO_2^-(aq) + 7H^+(aq) + 6e^- \rightarrow$$
$$NH_3(g) + 2H_2O(l) \quad U^\circ = +0.792 \; V_{RHE} \quad (6)$$

$$NO_3^-(aq) + 9H^+(aq) + 8e^- \rightarrow$$
$$NH_3(g) + 3H_2O(l) \quad U^\circ = +0.799 \; V_{RHE} \quad (7)$$

At pH = 14:

$$NO_2^-(aq) + 5H_2O(l) + 6e^- \rightarrow$$
$$NH_3(g) + 7OH^-(aq) \quad U^\circ = -0.173 \; V_{SHE,pH\,=\,14} \quad (8)$$

$$NO_3^-(aq) + 6H_2O(l) + 8e^- \rightarrow$$
$$NH_3(g) + 9OH^-(aq) \quad U^\circ = -0.132 \; V_{SHE,pH\,=\,14} \quad (9)$$

In recent work from our research group, Choueiri et al. identified the possibility of oxygenated intermediates on β-Ni(OH)$_2$ (ref. 36) and β-NiOOH.[39] Although these studies have identified dinitrogen as a primary product through the G–M mechanism, the presence of oxygenated intermediates presents subsequent reaction pathways involving oxygenated species. Through the mechanism of the formation of nitrite and nitrate, various oxygenated intermediates are made possible through the reaction between nitrogen-containing species and hydroxide molecules, as seen in Fig. 2.[23,39] One of these important intermediate species is nitric oxide (NO).[23] The reduction reaction of NO to ammonia can be seen in eqn (11), and it is a five electron reaction.

$$NO(aq) + 5H^+(aq) + 5e^- \rightarrow$$
$$NH_3(g) + H_2O(l) \quad U^\circ = +0.707 \; V_{RHE} \quad (10)$$

At pH = 14:

$$NO(aq) + 4H_2O(l) + 5e^- \rightarrow$$
$$NH_3(g) + 5OH^-(aq) \quad U^\circ = -0.121 \; V_{SHE,pH\,=\,14} \quad (11)$$

The production of NO adds another branch to the overall AOR, as further reactions between AOR intermediates and NO may exist, leading to the formation of by-products such as N$_2$O, also seen in Fig. 2.[32–34,40–43] The reaction to form N$_2$O has been shown to occur through a Langmuir–Hinshelwood type recombination reaction.[43,44] This interaction may occur between
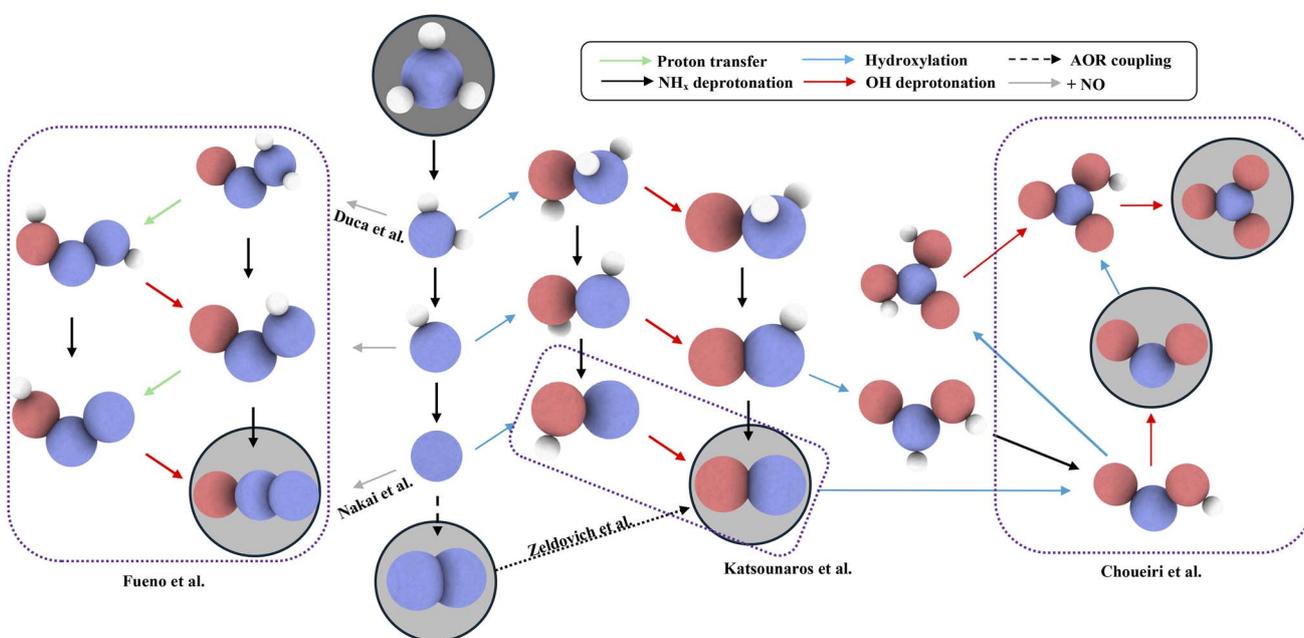

Fig. 2 Diagram of proposed AOR pathways that include oxygenated intermediates and mechanisms. The dotted purple boxes outline mechanisms that have previously been discovered to occur along the AOR, explored by Fueno et al.,[32] Duca et al.,[33] Nakai et al.,[34] Zeldovich et al.,[35] Katsounaros et al.,[23] and Choueiri et al.[36] Species outlined in the light gray circles are potential products that are released from these mechanisms seen on various metals and surfaces.

Table 1 Comparison of Gibbs free energies of reaction calculated from experimental values and their corresponding DFT calculations at pH 11 for potential products that could exist during the electro-catalytic AOR. Thermodynamic values for each species can be found in Lange's *Handbook of Chemistry*[45]

Products	Thermodynamic $\Delta_r G$ (eV)	DFT $\Delta_r G$ (eV)	Error (eV)
N_2	+3.56	+3.45	−0.11
NO	−0.28	−0.33	−0.05
NO_2^-(aq)	−0.20	−0.36	−0.16
NO_3^-(aq)	−0.53	−0.63	−0.10
N_2O	+1.33	+1.19	−0.14
N_2H_4	−0.60	−0.69	−0.09

AOR intermediates and *NO to form coupled species that could eventually lead to N_2O(g) on the surface.[34,42,43] Additionally, nitric oxide can be formed through a high temperature combustion reaction between dinitrogen and oxygen, known as the Zeldovich mechanism.[35] The existence of NO molecules has been observed in multiple studies that investigate AOR, and is considered an important intermediate molecule towards the production of NO_2^-(aq) and NO_3^-(aq).[23,27] Table 1 summarizes both experimentally reported and DFT-calculated Gibbs free energy of reaction for the various products that could be produced through AOR pathways at pH 11, which show good agreement. The experimental values were obtained by calculating the thermodynamic Gibbs free energy of reaction using the standard Gibbs free energies of formation for each species, as reported in Lange's *Handbook of Chemistry*.[45] An example calculation for the Gibbs energy of reaction is outlined by Choueiri *et al.* in their ESI.†[36] The DFT values were calculated using the gas phase values for each species and the product energies were corrected using their associated gas phase errors as outlined by Urrego-Ortiz, *et al.*[46] These corrections were employed to address deviations in DFT calculations, specifically with N–O bonds,[46–48] and were employed throughout this study. By using these gas-phase corrections, we were able to reduce the difference between thermodynamic and DFT values to below $|0.2|$ eV.

The thermodynamic equilibrium potentials (U) for the prospective products through electro-catalytic AOR can be seen in Fig. 3. These equilibrium potentials have been summarized for the reduction of nitrogen-containing products at pH 0 and 14. This study will provide insight into the mechanism by which AOR proceeds upon electro-oxidation. Since our research group has previously investigated β-Ni(OH)$_2$ and β-NiOOH, studying NiO will extend our understanding of nickel-based surfaces and their reactivity towards AOR.[36,39] It has also been reported in the literature that NiO co-exists with β-Ni(OH)$_2$ in nature, and as the potential and pH approach AOR conditions, NiO becomes the thermodynamically favoured surface.[49] Building on this, NiO is currently underexplored despite its existence under favourable AOR conditions. To address this, we utilize density functional theory (DFT) to analyze the catalytic behavior of NiO by determining surface parameters, identifying adsorption sites, and calculating free energy diagrams (FEDs) to assess AOR
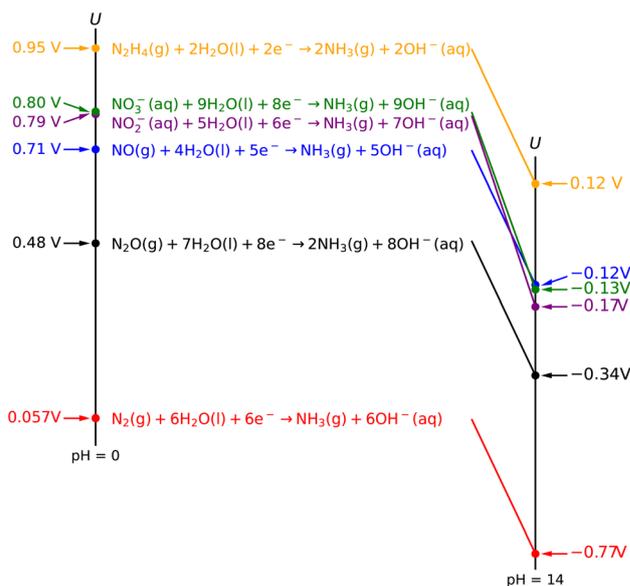
Fig. 3 Thermodynamic equilibrium potentials (U) at pH 0 and pH 14 for the various reduction reactions of nitrogen-containing products.

mechanisms. By investigating NiO, we aim to further understand nickel-based materials and how they behave when catalyzing AOR.

2 Computational methods

All DFT calculations were conducted using the Vienna *Ab initio* Simulation Package (VASP, version 5.4.4)[50–52] while using the atomic simulation environment (ASE) to run, analyze, and visualize the results.[53] The RPBE functional[54] was applied to account for the electronic interactions in the system and the core electrons were treated with pseudopotentials derived from the projector augmented wave (PAW) approach provided with VASP.[55,56] The generalized gradient approximation with Hubbard U correction potential (GGA + U) is used to correct overdelocalization of Ni d-electrons.[57,58] The Hubbard U value was chosen based on agreement with previous computational studies and experimental reports on NiO.[59–63] The Hubbard U is further discussed in the NiO Bulk Analysis section of this paper. The experimentally determined NiO bulk structure (mp-19009)[64] was obtained from the Materials Project.[65] For geometry optimizations, the planewave cutoff is set to 500 eV and a Monkhorst–Pack k-point mesh of ($4 \times 4 \times 1$) is used to sample the Brillouin zone.[66] For the bare slab surface, the bottom two layers are fixed in their positions while the top two layers were allowed to relax and reach their lowest energy geometry. The optimized unit cell can be seen in Fig. 4. All structures are optimized until forces on all free atoms are less than 0.05 eV Å^{-1}. The free energy of each species is obtained using the following equations:

$$H = E_{\text{electronic}} + \text{ZPE} + \int_0^T C_p \mathrm{d}T \qquad (12)$$
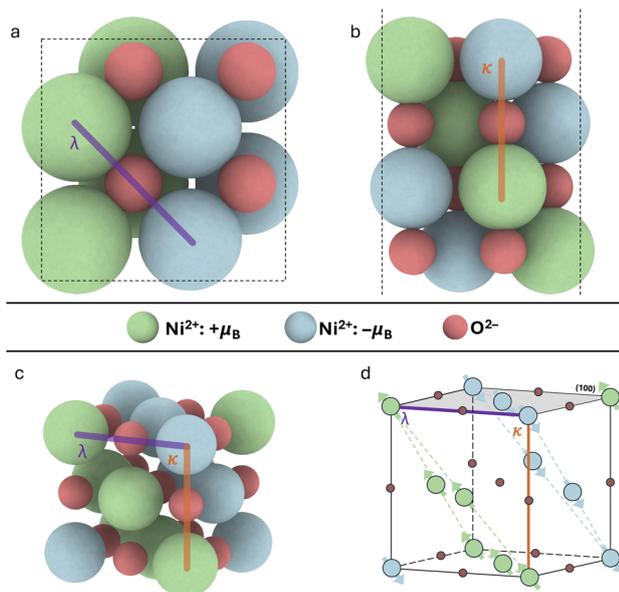
Fig. 4 Top (a) and side (b) views of the NiO(100) surface used in this study, where (a and b) represent the pristine NiO surface used for the calculations. A visual of the (111) AFM layering is presented in (c and d).

$$G = H - TS \qquad (13)$$

These thermochemical corrections were calculated under the ideal-gas limit for gas-phase molecules and the harmonic limit for adsorbates. The FEDs were constructed using the Gibbs free energies for each intermediate, referenced to the pristine slab, $NH_3(g)$, $H_2(g)$, and $H_2O(l)$. Each FED used the lowest calculated adsorption free energy for each intermediate in each reaction pathway. All Gibbs free energies are referenced to pH 11 and the stated applied potential using the computational hydrogen electrode (CHE) developed by Nørskov et al.[67] and adapted by Chen et al. for alkaline environments.[68] The free energies of desorption for aqueous nitrite and nitrate are derived from thermodynamic cycles based on their respective acids. The DFT-calculated electronic energies and corresponding thermochemical corrections are provided in the ESI.†

While the current study focuses on the thermodynamic properties of AOR on a NiO surface, we can identify thermodynamically favorable pathways and potential-determining steps. Based on the Brønsted–Evans–Polanyi (BEP) relationship, we can relate the thermodynamically limiting step with the rate-determining step, as steps with higher reaction free energies tend to exhibit higher activation barriers.[69,70] Through this relation, identification of the potential-determining step can provide an approximation of the rate-limiting step.[69,70] However, the absence of kinetic analysis represents a limitation of this study and relying solely on thermodynamic data does not capture the entire catalytic behavior of the NiO surface. Future studies involving kinetic modeling would offer further understanding of the AOR mechanism and should be investigated.

3 Results and discussion

3.1 NiO bulk analysis

A comprehensive bulk analysis was performed to establish the understanding of NiO and its properties. Calculating the band gap, lattice parameter(s), and magnetic moment(s) is crucial for accurately representing the material. Experimentally, NiO has a band gap of 3.4 eV and a lattice parameter that ranges from 4.17–4.195 Å.[71,72] The magnetic structure of NiO was previously determined by neutron diffraction, revealing antiferromagnetic (111) sheets.[73] The antiferromagnetic layering of Ni atoms in NiO can be seen in Fig. 4. Furthermore, local magnetic moments of the nickel atoms can range from 1.64 to $1.77\mu_B$.[74] The band gap, lattice parameter, and local magnetic moment of the NiO bulk structure were calculated in a previous study by Rohrbach et al.,[59] who used various DFT methods to calculate the bulk properties of NiO, including LSDA, SGGA, LSDA + U, and SGGA + U.[59] It was found that a Hubbard U correctional value of $U = 6.3$ eV is required to accurately represent NiO and reproduce its experimental bulk properties.[71,72,74,75] The current study investigated the effect of varying Hubbard U values on the bulk properties which can be seen in Fig. 5. These results agreed well with the trends seen in the research conducted by Rohrbach et al.[59] Using a value of $U = 6.3$ eV our calculations yielded a bulk NiO lattice parameter of 4.23 Å, a local magnetic moment of $1.76\mu_B$, and a band gap of 3.35 eV, all in reasonable agreement with experimental values.[71,72,74,75]

The Ni Pourbaix diagram is shown in Fig. 6, highlighting the thermodynamically stable phases across varying pH values and potentials.[49] As previously stated, it can be seen that NiO, $Ni(OH)_2$, and NiOOH exist in regions where AOR catalysis can occur.[49] Investigating these Ni phases allows us to further understand Ni-based materials as model surfaces for studying AOR catalysis.
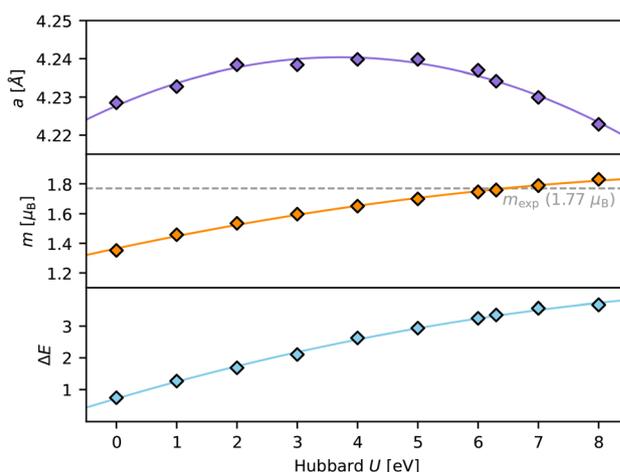

Fig. 5 Lattice constant (a), magnetic moment (m), and band gap (ΔE) calculated for the NiO surface using a range of Hubbard U values from 0–8. The Hubbard U value was chosen based on the closest match to experimental values for the magnetic moment.[74] However, the calculated band gap and lattice parameter also agree with experimental values of NiO.
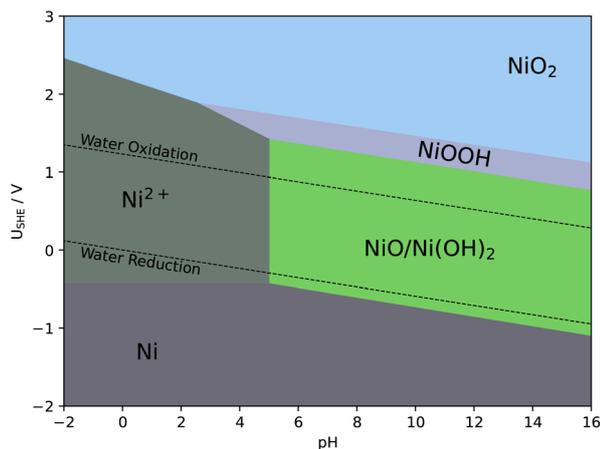
Fig. 6 Density-functional theory (DFT) Ni Pourbaix diagram. The two parallel broken lines represent the potentials for the oxidation and reduction of water. Adapted with permission from L. F. Huang, M. J. Hutchinson, R. J. J. Santucci, J. R. Scully and J. M. Rondinelli, *The Journal of Physical Chemistry C*, 2017, **121**, 9782–9789. Copyright 2017 American Chemical Society.[49]

3.2 NiO surface analysis

The NiO surface has been used for the investigation of adsorption characteristics with various molecules including syngas.[62,76–78] Specifically, the (100) facet is often used due to its thermodynamic stability.[79] Building on this understanding, our study focuses on utilizing the NiO (100) surface to conduct catalysis. It has also been reported that the surface energies increase in order of (100), (110), and (111).[79]

Surface defects in the form of vacancies are commonly investigated as they can alter the catalytic performance of the surface.[80,81] Typically, investigations on vacancies focus on the removal of oxygen as metal vacancies require higher energy and could destabilize the surface.[80,81] Previous work by Choueiri *et al.* on β-NiOOH showed that vacancies existed under AOR conditions.[39] In their study, hydroxide vacancies were found to be favoured below $U = 0.69$ V$_{SHE}$, still within the range of interest of AOR, while oxygen vacancies were formed at less positive potentials.[39] Therefore, it was determined that investigating both vacancies was crucial for understanding the catalysis of ammonia oxidation on the surface of β-NiOOH.[39]

$$**O + 2H^+(aq) + 2e^- \rightarrow H_2O(l) + ** \quad (14)$$

Building on these findings, the current study focuses solely on oxygen vacancies and their ability to form under AOR conditions. The chemical equation outlining the vacancy formation is presented in eqn (14), where **O represents the intact surface (*i.e.* the oxygen atom is remains adsorbed on the future vacancy site) and ** represents the surface with an oxygen vacancy.

Free energies were obtained using DFT calculations of the pure-surface and vacancy-containing NiO. The reaction scheme for determining the free energy of vacancy formation on NiO can be seen in eqn (15).

$$\Delta G_O(pH, U) = (\mu_{H_2O} + E_{**}) \\ - (E_{**O} + \mu_{H_2} - 2eU - 0.1183pH) \quad (15)$$

As shown in Fig. 7a, oxygen vacancy formation is only favoured below $U_{SHE} = -0.9$ V for acidic environments, and below $U_{SHE} = -1.4$ V under alkaline conditions. Typically, AOR occurs at positive potentials and under alkaline conditions, meaning that oxygen vacancies are not expected to form on the pristine NiO surface during catalysis. Therefore, unlike β-NiOOH, the pristine NiO surface is a sufficient model for investigating AOR catalysis.

Another surface alteration which may occur on the NiO surface is the possibility of protonating the lattice oxygens, resulting in surface hydroxylation. To assess this, a stability diagram was also constructed to determine the possibility of eqn (16), under various electrochemical conditions.
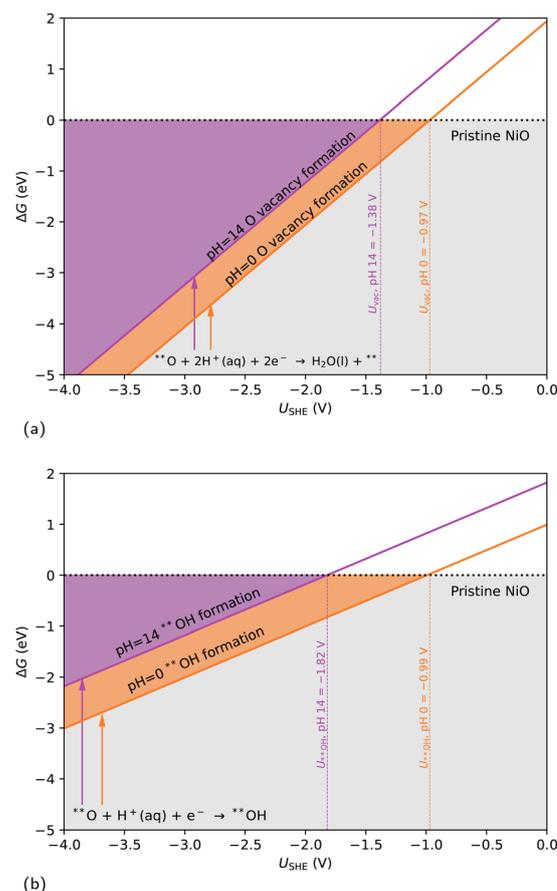
$$**O + H^+(aq) + e^- \rightarrow **OH \quad (16)$$

(a)

(b)

Fig. 7 Surface stability diagrams of NiO under different surface alterations. (a and b) Free energy of oxygen vacancy formation and lattice oxygen protonation, respectively. The surface stability diagrams were plotted as a function of the applied potential at pH 0 and pH 14. In both cases, the surface modifications become favorable at negative potentials, which lie outside the AOR conditions. This indicates that the pristine NiO surface will remain stable during the AOR. (a) Free energy of the NiO slab with one oxygen vacancy, where the vacancy formation reaction energy is plotted as a function of potential at pH 0 and pH 14. (b) Free energy of the NiO slab with one protonated lattice oxygen, where the lattice oxygen protonation reaction energy is plotted as a function of potential at pH 0 and pH 14.

As shown in Fig. 7b, similar to vacancy formation, hydroxylation of lattice oxygen becomes favorable at lower potentials. Therefore, surface hydroxylation is not expected to occur under AOR conditions. However, when comparing the hydroxylation and vacancy formation on the surface, it can be seen that at pH = 0, both alterations become favorable at the same potential. However, as the pH increases, the vacancy formation becomes the dominant alteration.

3.3 Site testing

The (100) facet of NiO presents four different adsorption sites:[78] Ni-atop, O-atop, bridge, and four-fold hollow, as shown in Fig. 8. In order to determine the favourable pathway for AOR on NiO, adsorption of the intermediate molecules was evaluated on the four sites. The initial tests were performed using an atomic nitrogen atom to analyze adsorption behaviour. It was observed that the Ni-atop site was the only location where the atomic nitrogen did not chemically react with a surface oxygen atom. The other three sites resulted in the formation of an NO intermediate species along with an oxygen vacancy, thus resulting in alternate reaction pathways. Based on this observation, it is important to test the different intermediates and determine their reactivity with the lattice oxygen. Furthermore, a comparison of nitrogen adsorption on Ni atoms possessing different magnetic moments was performed. Since a (111) AFM layering exists within the NiO surface, it results in two different-magnetic moment Ni atoms on the (100) face. It was found that nitrogen adsorption on the Ni site with a negative magnetic moment resulted in a reduction in energy by 0.25 eV, suggesting enhanced stability. The lowest energy adsorption sites for each species were determined and used to construct the free-energy diagrams, allowing for a comprehensive understanding of the mechanistic pathways.
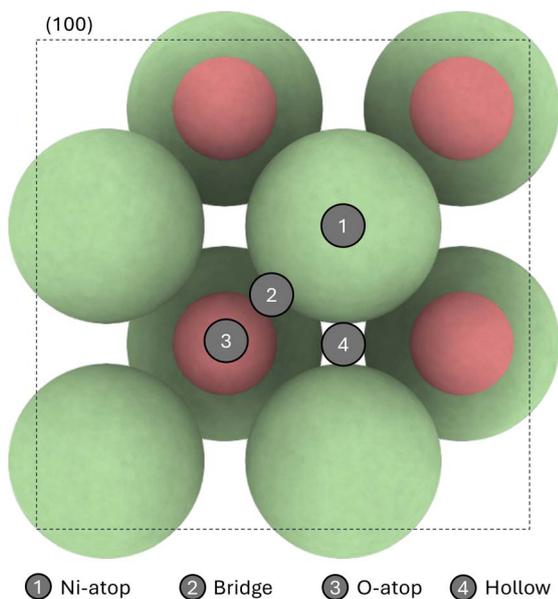

Fig. 8 Adsorption sites that were tested in this study. The (100) NiO surface has four different sites: Ni-atop, bridge, O-atop, and a four-fold hollow.

Unlike Ni-atop site tests, almost all intermediate molecules did not adsorb on the O-atop site tests with the sole exception of the nitrogen atom, which formed the aforementioned NO intermediate with a lattice oxygen atom. Approximately half of the intermediate molecules from the bridge site tests stayed adsorbed, while most of the intermediate molecules from the four-fold hollow site stayed adsorbed.

Hydrogen-containing intermediates that were unable to adsorb during geometry optimization were repositioned with the hydrogen atoms brought closer to the lattice oxygens before rerunning the geometric optimization; for the majority of these intermediates, the previously desorbed intermediates successfully adsorbed on the NiO surface, indicating that hydrogen bonding played a key role in intermediate adsorption.

3.4 NiO electrocatalysis

The FEDs in the subsequent sections were constructed using the Gibbs free energies for each intermediate, referenced to the pristine slab, $NH_3(g)$, $H_2(g)$, and $H_2O(l)$. Each FED uses the lowest calculated adsorption free energy for each intermediate in each reaction pathway.

3.4.1 Dinitrogen-containing products. $N_2(g)$ is commonly referred to as a primary product of AOR. On the NiO surface, the adsorption energy of ammonia was calculated to be 0.12 eV. This energy differs from previous findings on $Ni(OH)_2$ and NiOOH reported by Choueiri et al., as the energy required for the adsorption on these surfaces is slightly more negative.[36,39] Although the adsorption energy of ammonia on the NiO surface is thermodynamically uphill under standard conditions, the adsorption energy can vary with the concentration of the ammonia precursor. With an increase in the concentration of ammonia, the chemical potential will also increase. As a result, the adsorption process becomes more favored. Another important consideration is the competitive adsorption of oxygen evolution reaction (OER) intermediates which may exist under similar oxidative conditions. Understanding the competitive nature of these two reactions is necessary to accurately predict NiO's catalytic activity under AOR conditions, which can be the topic for a future study.

In order to investigate the preferred mechanism of AOR on NiO, we start by comparing the equilibrium (U_{eq}) and limiting potentials (U_{lim}) required for both the Oswin–Salomon and Gerischer–Mauerer mechanisms. As mentioned previously, the O–S mechanism leads to the formation of dinitrogen through six deprotonation steps before the coupling of the atomic nitrogen atoms. Alternatively, the G–M mechanism involves coupling after any of the deprotonation steps of ammonia to form various coupled intermediates that will then undergo further deprotonation.

After calculating the free energies of each intermediate from the O–S and G–M mechanisms of AOR, we are able to establish the equilibrium (U_{eq}) and limiting potentials (U_{lim}). The FEDs for the O–S and G–M mechanisms are seen in Fig. 9 and 10, respectively. In both cases, the initial deprotonation from *NH_3 to *NH_2 was found to be the potential determining step. Since the U_{lim} is the same for both mechanisms, it can be determined
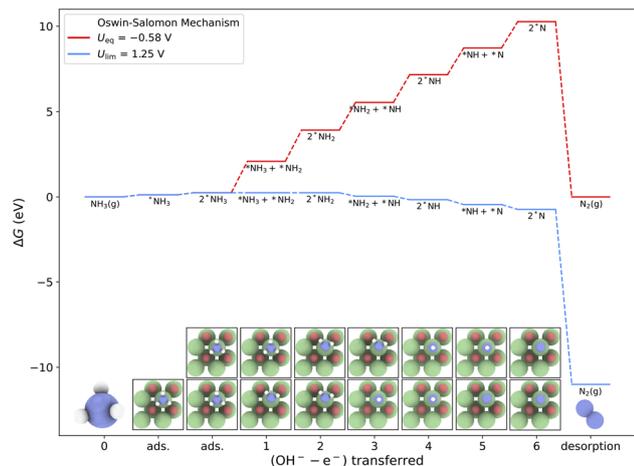
Fig. 9 Free energy diagram of $N_2(g)$ formation from AOR coupling through two *N intermediates (Oswin–Salomon mechanism).[37] Equilibrium (red trace) and limiting (blue trace) potentials are calculated using the computational hydrogen electrode at pH 11.

that both pathways are possible under the same applied potential. However, upon further examining the individual steps for both mechanisms, it can be determined that the G–M mechanism is slightly favoured due to the second highest required applied potential. For the O–S mechanism, the *NH_2 to *NH deprotonation step requires the second highest applied potential, which is calculated to be 1.04 eV. It is also worth mentioning that after each sequential deprotonation step, the minimum applied potential decreases. In contrast, the second highest required applied potential in the G–M mechanism corresponds to the deprotonation step from *NH_2–NH_2 to *NH–NH_2, which requires only 0.06 eV. This difference suggests that, although both AOR mechanisms are possible to proceed under the same applied potential, the G–M mechanism is slightly favoured. Additionally, it was observed that the desorption of
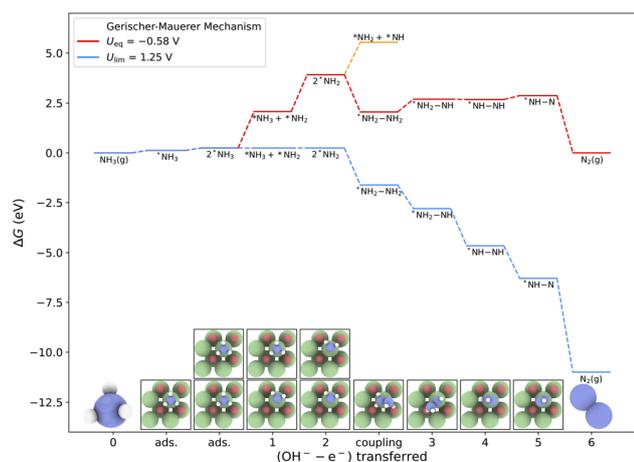
*N_2H_4 from the NiO surface is energetically favourable; however, the deprotonation steps become lower in energy with the applied potentials. These findings align with the previous studies on NiOOH and Ni(OH)$_2$, demonstrating that the AOR G–M mechanism is preferred on the nickel-based surfaces. However, the NiO surface displays an earlier coupling step, between two *NH_2 intermediates, compared to the previously studied surfaces, where the coupling occurred between two *NH intermediates.[36,39]

An area worth investigating is the production of hydrazine. As mentioned above, hydrazine has been identified as the potential product produced through AOR on NiO. The thermodynamic equilibrium potential is more positive in comparison to dinitrogen formation. The limiting potential, however, is consistent with dinitrogen, as the first deprotonation step from *NH_3 to *NH_2 remains the limiting step. This suggests that hydrazine will form in competition with dinitrogen under experimentally relevant potentials. The FED for the formation of hydrazine can be seen in Fig. 11.

3.4.2 Nitric oxide formation. For the formation of nitrite and nitrate, the preferred pathway is to proceed through NO. Since this is a common product formed by Ni-based catalysts in the literature, it is an important mechanistic step in determining the favoured pathway. The calculated desorption energy for NO(g) is −0.080 eV, meaning that NO is likely to be formed through the same applied potential. It is worth mentioning that the hydroxylation of *NH_2 to form *NH_2OH is thermodynamically more favourable in comparison to its deprotonation towards *NH, meaning that hydroxylation is likely to occur before the second deprotonation step. The FED for NO formation on the pristine surface is shown in Fig. 12. Furthermore, when investigating the formation of NO, it can also be seen that it can be formed through interaction with the lattice oxygen, which will be discussed in further detail in a later section. With
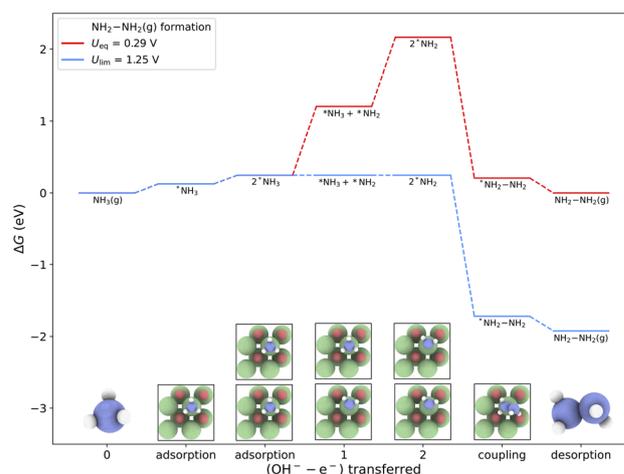

Fig. 10 Free energy diagram of $N_2(g)$ formation from AOR coupling through two *NH_2 intermediates (Gerischer–Mauerer mechanism).[38] Equilibrium (red trace) and limiting (blue trace) potentials are calculated using the computational hydrogen electrode at pH 11.

Fig. 11 Free energy diagram of hydrazine (N_2H_4) formed through the coupling between two *NH_2 intermediates. This mechanism avoids the deprotonation steps to form *NH and *N. Energy of desorption is calculated to be −0.25 eV. Equilibrium (red trace) and limiting (blue trace) potentials are calculated using the computational hydrogen electrode at pH 11.
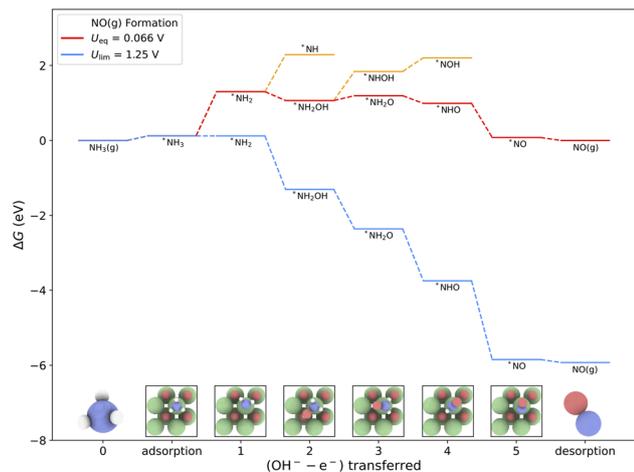
Fig. 12 Free energy diagram of NO(g) formation. This pathway includes the same initial steps of nitrite and nitrate formation, proceeding through *NH$_2$OH. Steps towards *NH and *NHOH are bypassed as their energies are less favoured. The desorption energy for NO(g) was calculated to be −0.080 eV. The equilibrium (red trace) and limiting (blue trace) potentials were calculated using the computational hydrogen electrode at pH 11.
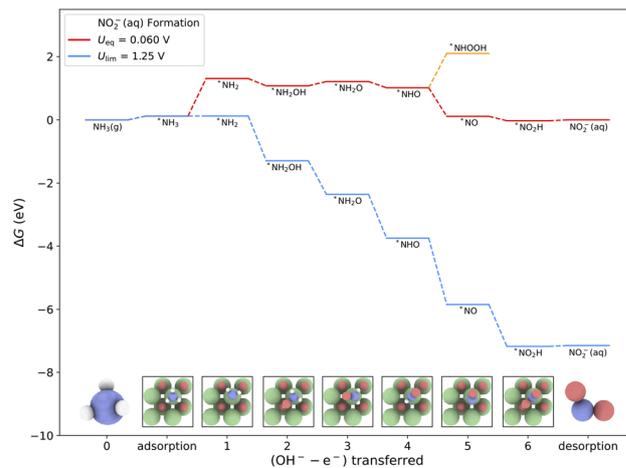
Fig. 13 Free energy diagram for NO$_2^-$(aq) formation. This pathway passes the deprotonation steps towards *NH and *N by hydroxylating *NH$_2$ to form *NH$_2$OH, which is energetically favourable. This pathway proceeds through *NHO and *NO, instead of potential branches to form *NOH or *NHOOH. The energy required for the final desorption step was calculated to be 0.027 eV. Equilibrium (red trace) and limiting (blue trace) potentials are calculated using the computational hydrogen electrode at pH 11.

this knowledge, we tested each adsorbate in close proximity to the lattice oxygen to see how they would behave.

3.4.3 Nitrite and nitrate formation. The formation of nitrite and nitrate species is also possible in the AOR. It has been observed that hydrogen bonds between the intermediate products and the lattice oxygens are necessary to promote adsorption and lower energies on the surface. Notably, the adsorption of *NH$_2$OH, *NO$_2$H, and *NO$_3$H was strongly influenced by the formation of hydrogen bonds with lattice oxygen atoms. Without the stabilizing effect of these hydrogen bonds, the intermediates are unable to adsorb on the surface in any other configuration.

After obtaining the most stable geometries of all intermediates, we were able to construct the FEDs for the formation of nitrite and nitrate seen in Fig. 13 and 14, respectively. Furthermore, it can be seen in Fig. 13, that the deprotonation of the oxygen atom on the adsorbate is likely to occur before the deprotonation of the nitrogen atom. As per the other mechanisms outlined in this research, the limiting step remains consistent across the formation of all by-products. However, in the case of nitrate formation, the deprotonation step from *NO$_2$H towards *NO$_2$ exhibits a similar limiting potential to the initial deprotonation from *NH$_3$ to *NH$_2$. Although nitric oxide is a possible product due to its favourable desorption energy as previously discussed, it is important to highlight the competing mechanistic step to form *NO$_2$H. With the applied potential, it is likely that *NO will continue following the oxygenated-pathway rather than desorbing from the surface.

To evaluate product formation on NiO, the desorption energies of aqueous nitrite and nitrate were examined. Under AOR conditions, the desorption energy for nitrite was calculated to be 0.027 eV, whereas the desorption energy of nitrate was calculated to be −0.029 eV. This suggests that NO$_3^-$(aq) is likely

to form and desorb from the surface under AOR conditions. Additionally, at pH 14, the desorption energy of NO$_2^-$(aq) becomes −0.15 eV, meaning that production of nitrite is likely when the pH is increased above AOR conditions. As a result, this reaction pathway is likely to proceed towards nitrate formation as each step in the reaction mechanism is downhill in energy under the applied limiting potential, including the desorption of NO$_3^-$(aq).
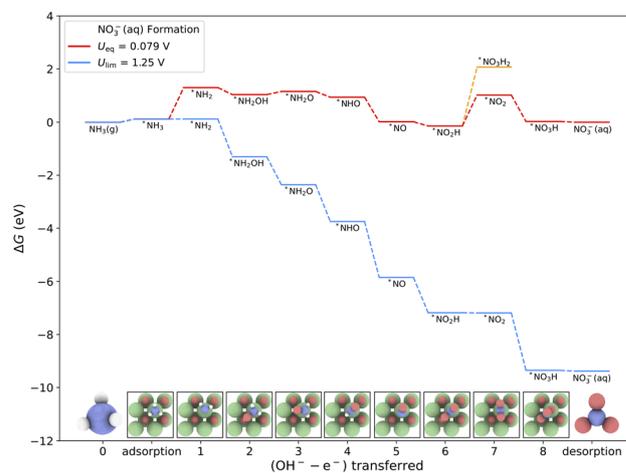

Fig. 14 Free energy diagram for NO$_3^-$(aq) formation by proceeding through the same mechanistic steps towards NO$_2^-$(aq). After *NO$_2$H is formed, the mechanism branches towards *NO$_2$ or *NO$_3$H$_2$, with the deprotonation step being energetically preferred. The energy required for the final desorption step was calculated to be −0.029 eV. Equilibrium (red trace) and limiting (blue trace) potentials are calculated using the computational hydrogen electrode at pH 11.

3.4.4 Nitrous oxide formation. The FED for $N_2O(g)$ formation on the pristine NiO surface (Fig. 15) shows the most favorable pathway to $N_2O(g)$. As with the other AOR intermediates, the limiting step is the initial deprotonation step from *NH$_3$ to *NH$_2$. Additionally, the hydroxylation of *NH$_2$ is thermodynamically more favorable than further deprotonation to *NH for *NO formation. From this step, different pathways can lead to $N_2O(g)$ formation. As presented in Fig. 2, *NH$_2$OH can undergo two deprotonation steps at the nitrogen atom to produce *NOH before coupling with *NH to form *HNNOH. While the formation of *HNNOH can be achieved through the intramolecular proton transfer between *H$_2$NNO and *HNNOH,[82] the absence of any electron transfer makes this step independent of potential. Thus, the coupling between *NOH and *NH was considered to avoid this step. However, further deprotonation steps from *HNNOH still require an applied potential to progress to $N_2O(g)$. In contrast, another pathway from *NH$_2$OH is the deprotonation from the oxygen, which was found to be more favorable compared to the previously discussed pathway. From *NH$_2$O, the subsequent deprotonation steps to *NO are thermodynamically downhill in energy.

*NO can couple with the AOR intermediate,: *NH$_2$ or *NH, prior to deprotonation to $N_2O(g)$.[32] However, the thermodynamics presented in Fig. 15 show that *N is the most favoured intermediate for coupling with *NO, indicating all deprotonation steps occur before the coupling of the two nitrogen atoms. In this favoured pathway, *NO and *N undergo Langmuir–Hinshelwood recombination to form $N_2O(g)$. Because $N_2O(g)$ is unable to adsorb on the NiO surface based on our DFT calculations, we can conclude that the coupling and desorption steps are concerted. Furthermore, any further reactions that may involve $N_2O(g)$ are unlikely to be catalyzed by NiO. Thus, the coupling of *NO and *N is a relatively novel pathway for $N_2O(g)$ formation, which has been supported by other DFT studies.[43]

3.4.5 Lattice oxygen pathways. The interaction between the lattice oxygen in NiO and the adsorbates demonstrates alternative pathways towards intermediate oxygenated species. The presence of lattice oxygen could influence product selectivity and promote favourable reaction mechanisms. All considered intermediates were tested for their reactivity with the lattice oxygen by positioning the adsorbate in close proximity to the oxygen. It was found that the pathway leading to nitrous oxide (N_2O), did not involve lattice oxygen interactions with the coupled intermediates. However, some possible reactions that could occur with the lattice oxygen involve the interaction between oxygen and the intermediates such as *N, *NH, and *NOH. These intermediates were capable of coupling with the lattice oxygen to form *NO, *NHO, and *NO$_2$H, respectively. As a result, the lattice oxygen is removed from the surface and becomes involved in the reaction pathway. This reaction creates an oxygen vacancy, altering the NiO surface. The formation of an oxygen vacancy can be described using these general equations:

$$*ad + **O_{lat} \rightarrow **ad - O_{lat} + * \tag{17}$$

$$**ad - O_{lat} \rightarrow ad - O(g) + ** \tag{18}$$
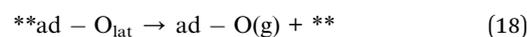
where *ad represents an adsorbed intermediate, **O$_{lat}$ represents the lattice oxygen in the site before the vacancy is formed, ** represents the surface with an oxygen vacancy, and * represents the original site of adsorption. Due to the presence of lattice oxygen on the surface, it is important to investigate the energies necessary for these pathways to occur. Comparison
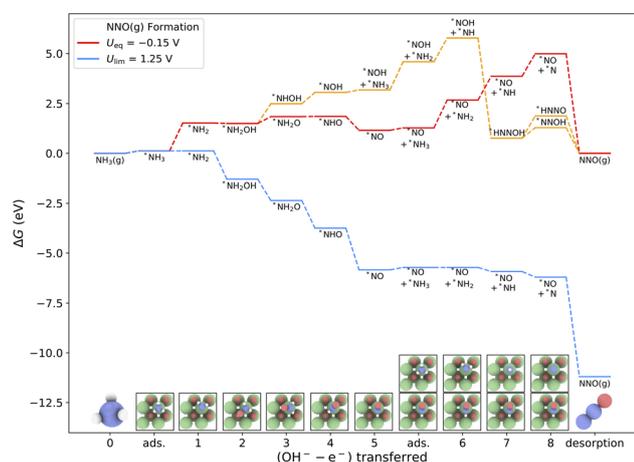
Fig. 15 Free energy diagram for $N_2O(g)$ formation by proceeding through the interaction between *NO and *N (Langmuir−Hinshelwood recombination). After *NH$_2$OH is formed, the mechanism branches towards *NHOH or *NH$_2$O, with the latter deprotonation step being energetically preferred. This pathway requires the subsequent deprotonation steps to form *N. Equilibrium (red trace) and limiting (blue trace) potentials are calculated using the computational hydrogen electrode at pH 11. The coupling between *NOH and *NH to avoid the thermodynamically unfavourable chemical step of the proton transfer is shown as well (orange trace).
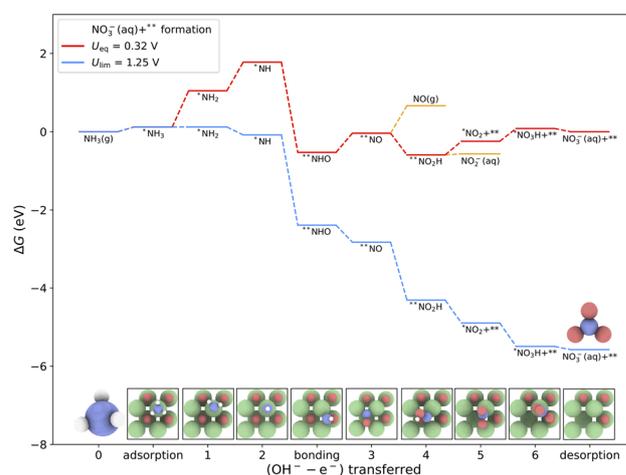
Fig. 16 Free energy diagram for NO(g), NO_2^-(aq), and NO_3^-(aq) formation by proceeding through the interaction between *N-containing intermediates and the lattice oxygen, **O$_{lat}$. The energies of desorption for NO(g), NO_2^-(aq), and NO_3^-(aq) were calculated to be +0.77, +0.19, and −0.74 eV, respectively. Equilibrium (red trace) and limiting (blue trace) potentials were calculated using the computational hydrogen electrode at pH 11.

between these pathways allows us to determine if the lattice oxygen plays a stabilizing role in the overall AOR on NiO.

The FED for the formation of NO(g), NO_2^-(aq) and NO_3^-(aq) was constructed and is shown in Fig. 16. From this diagram, it can be seen that these pathways share the same limiting step as the other discussed mechanisms: the deprotonation of $*NH_3$ to $*NH_2$. In contrast to the other pathways, further deprotonation towards $*NH$ or $*N$ is required to proceed through the lattice oxygen pathways as $*NH_2$ does not react with lattice oxygen. However, once $*NH$ is formed, it is highly favoured to react with the lattice oxygen to form $*NHO$ and proceed through the oxygenated mechanism while in the presence of a vacancy. Furthermore, these FEDs reveal that the desorption of NO(g) and NO_2^-(aq) is thermodynamically unfavourable due to their respective desorption energies of 0.70 eV and 0.025 eV. However, the desorption energy of NO_3^-(aq) is favourable in the presence of an oxygen vacancy in the lattice as the energy required is −0.083 eV. This suggests that NO_3^-(aq) is likely to form through this mechanism.

4 Conclusion

Building upon previous studies in our research group which investigated nickel hydroxide and nickel oxyhydroxide surfaces, the current work advances our understanding of nickel-based catalysts by focusing solely on nickel oxide in ammonia oxidation.

The NiO surface has been shown to potentially release a variety of products: N_2(g), N_2H_4(g), NO(g), N_2O(g), NO_2^-(aq), and NO_3^-(aq). The first step in the formation of all of these products is the chemisorption of NH_3(g) on the surface which requires +0.12 eV. Although this step is thermodynamically uphill, the Gibbs energy of adsorption can be controlled using different concentrations of NH_3(g). Furthermore, all products share the same potential-limiting step, which occurs during the first deprotonation of ammonia from $*NH_3$ to $*NH_2$. The respective limiting potential for this step is +1.25 V, for all products discussed in this work.

For dinitrogen formation, the NiO surface is shown to slightly favour the G–M mechanism compared to the O–S mechanism. On the NiO surface, the preferred coupling occurs between two $*NH_2$ intermediates to form $*N_2H_4$. It can be seen that the coupling step between two $*NH_2$ intermediates is considerably downhill compared to the subsequent deprotonation step towards $*NH$. It is worth mentioning that the coupling step occurs earlier on the NiO surface compared to the previously studied surfaces in our research group where coupling occurred between two $*NH$ adsorbates,[36,39] requiring an additional deprotonation step. There is evidence that the formation of N_2H_4 on the surface could be the final step in the reaction as the desorption could occur spontaneously since the energy is downhill, being −0.25 eV. The competing reaction is the deprotonation towards $*N_2H_3$ which will proceed to the desorption of dinitrogen.

Another possible pathway for ammonia is the formation of oxidized species. The first two steps remain the same as the dinitrogen formation, through the initial chemisorption and the deprotonation to $*NH_2$. After this step, the hydroxylation

towards $*NH_2OH$ is likely to occur before the deprotonation to $*NH$ as the energy is 1.21 eV lower for the hydroxylation step. This hydroxylation step is then followed by a subsequent deprotonation step before the nitrogen undergoes further deprotonation. This route remains the same for the formation of NO(g), NO_2^-(aq), and NO_3^-(aq). When calculating their relative desorption energies, it can be seen that NO(g) and NO_3^-(aq) have favourable energies, whereas, under AOR conditions, NO_2^-(aq) has been calculated to have an unfavourable energy. This suggests that through the oxygenated pathway, NO(g) and NO_3^-(aq) are likely products. However, due to intermediate energies in the oxygenated-pathway, it is likely that $*NO$ will proceed towards $*NO_2H$ instead of desorbing from the surface with the applied potential. Additionally, all the steps leading to the formation of N_2O proceed downhill after the original limiting step, seen in all cases.

Although the production of NO(g) is possible, it can also interact with AOR intermediates. The interaction on the surface between $*NO$ and $*N$ can lead to the formation of N_2O(g). However, while both $*NO$ and $*N$ can form on the surface at the applied potential, they are likely to undergo subsequent oxidation steps. This decreases the likelihood of their coexistence and makes the formation of N_2O(g) unlikely. NiO is capable of initiating new reaction pathways not seen on hydroxide or oxyhydroxide surfaces, through interactions between lattice oxygen and intermediates. Through DFT calculations, it has been shown that $*NH$, $*N$, and $*NOH$ can couple with lattice oxygen to form $*NHO$, $*NO$, and $*NO_2H$ respectively. Although spontaneous oxygen vacancy formation during AOR conditions is not favoured on the NiO surface, the interaction of intermediates with the lattice oxygen allows the creation of oxygen vacancies on the surface. Furthermore, this pathway is likely to proceed to the desorption of NO_3^-(aq) as the desorption energies for both NO(g) and NO_2^-(aq) are unfavourable as the desorption energies are 0.71 and 0.025 V, respectively.

While this research focuses solely on the catalytic activity of pristine NiO, a future direction that is worth investigating is the role of metal dopants. Previous studies have shown that doping NiO with noble metals such as Pt or Pd, could enhance the catalytic activity of the surface.[83,84] Such modifications and their comparison to the current work will provide valuable insight for a more detailed understanding of NiO's catalytic ability toward AOR.

These findings advance our understanding of AOR on nickel-based and metal oxide catalysts. These insights will guide the design of more efficient and selective AOR catalysts for various applications.

Data availability

The code for the Vienna *Ab initio* Simulation Package can be purchased at **https://www.vasp.at**. The version of the code employed for this study is version 5.4.4.

Conflicts of interest

There are no conflicts to declare.

Acknowledgements

Notes and references

1 F. Barbir, T. Veziroğlu and H. Plass, *Int. J. Hydrogen Energy*, 1990, **15**, 739–749.

2 D. J. Soeder, in *Fossil Fuels and Climate Change*, Springer International Publishing, Cham, 2021, pp. 155–185.

3 A. Farnoosh, in *Power Generation from Coal, Oil, Gas, and Biofuels*, ed. M. Hafner and G. Luciani, Springer International Publishing, Cham, 2022, pp. 111–130.

4 A. Olabi, K. Elsaid, K. Obaideen, M. A. Abdelkareem, H. Rezk, T. Wilberforce, H. M. Maghrabie and E. T. Sayed, *Int. J. Thermofluids*, 2023, **20**, 100498.

5 T.-Z. Ang, M. Salem, M. Kamarol, H. S. Das, M. A. Nazari and N. Prabaharan, *Energy Strategy Rev.*, 2022, **43**, 100939.

6 J. Incer-Valverde, A. Korayem, G. Tsatsaronis and T. Morosuk, *Energy Convers. Manage.*, 2023, **291**, 117294.

7 M. Yue, H. Lambert, E. Pahon, R. Roche, S. Jemei and D. Hissel, *Renewable Sustainable Energy Rev.*, 2021, **146**, 111180.

8 B. Shadidi, G. Najafi and T. Yusaf, *Energies*, 2021, **14**, 6209.

9 M. K. Singla, P. Nijhawan and A. S. Oberoi, *Environ. Sci. Pollut. Res.*, 2021, **28**, 15607–15626.

10 M. Aminudin, S. Kamarudin, B. Lim, E. Majilan, M. Masdar and N. Shaari, *Int. J. Hydrogen Energy*, 2023, **48**, 4371–4388.

11 L. Fan, Z. Tu and S. H. Chan, *Energy Rep.*, 2021, **7**, 8421–8446.

12 Y. Liu, Z. Pan, O. Esan, X. Xu and L. An, *Energy Fuels*, 2022, **36**, 13203–13211.

13 Y. Huang, J. H. Feng, Y. Yi, F. Duan, X. Liu, G. Tian, J. Gu, H. Bian and J. Li, *Rare Met.*, 2025, **44**, 3686–3708.

14 A. Chien, W. Chen and M. Zheng, *J. Electrochem. Soc.*, 2023, **170**, 044505.

15 P. Vanysek, *CRC Handbook of Chemistry and Physics*, 2000, vol. 8, pp. 8–33.

16 A. De Vooys, M. Koper, R. Van Santen and J. Van Veen, *J. Electroanal. Chem.*, 2001, **506**, 127–137.

17 B. K. Boggs, R. L. King and G. G. Botte, *Chem. Commun.*, 2009, 4859–4861.

18 D. A. Finkelstein, E. Bertin, S. Garbarino and D. Guay, *J. Phys. Chem. C*, 2015, **119**, 9860–9878.

19 S. W. Wallace, I. T. McCrum and M. J. Janik, *Catal. Today*, 2021, **371**, 50–57.

20 G. Novell-Leruth, J. M. Ricart and J. Pérez-Ramírez, *J. Phys. Chem. C*, 2008, **112**, 13554–13562.

21 V. Rosca and M. T. Koper, *Phys. Chem. Chem. Phys.*, 2006, **8**, 2513–2524.

22 G. Novell-Leruth, A. Valcárcel, A. Clotet, J. Ricart and J. Perez-Ramirez, *J. Phys. Chem. B*, 2005, **109**, 18061–18069.

23 I. Katsounaros, M. C. Figueiredo, F. Calle-Vallejo, H. Li, A. A. Gewirth, N. M. Markovic and M. T. Koper, *J. Catal.*, 2018, **359**, 82–91.

24 F. J. Vidal-Iglesias, N. Garcia-Araez, V. Montiel, J. Feliu and A. Aldaz, *Electrochem. Commun.*, 2003, **5**, 22–26.

25 F. J. Vidal-Iglesias, J. Solla-Gullón, P. Rodrıguez, E. Herrero, V. Montiel, J. Feliu and A. Aldaz, *Electrochem. Commun.*, 2004, **6**, 1080–1084.

26 F. J. Vidal-Iglesias, J. Solla-Gullón, V. Montiel, J. M. Feliu and A. Aldaz, *J. Phys. Chem. B*, 2005, **109**, 12914–12919.

27 H. S. Pillai and H. Xin, *Ind. Eng. Chem. Res.*, 2019, **58**, 10819–10828.

28 N. J. Bunce and D. Bejan, *Electrochim. Acta*, 2011, **56**, 8085–8093.

29 A. Kapałka, A. Cally, S. Neodo, C. Comninellis, M. Wächter and K. M. Udert, *Electrochem. Commun.*, 2010, **12**, 18–21.

30 Y.-J. Shih, Y.-H. Huang and C. Huang, *Electrochim. Acta*, 2018, **263**, 261–271.

31 W. Xu, R. Lan, D. Du, J. Humphreys, M. Walker, Z. Wu, H. Wang and S. Tao, *Appl. Catal., B*, 2017, **218**, 470–479.

32 T. Fueno, M. Fukuda and K. Yokoyama, *Chem. Phys.*, 1988, **124**, 265–272.

33 M. Duca, M. C. Figueiredo, V. Climent, P. Rodriguez, J. M. Feliu and M. T. Koper, *J. Am. Chem. Soc.*, 2011, **133**, 10928–10939.

34 I. Nakai, H. Kondoh, T. Shimada, M. Nagasaka, R. Yokota, K. Amemiya, H. Orita and T. Ohta, *J. Phys. Chem. B*, 2006, **110**, 25578–25581.

35 J. Zeldovich, *Eur. Phys. J. A*, 1946, **21**, 577–628.

36 R. M. Choueiri, S. W. Tatarchuk, A. Klinkova and L. D. Chen, *Electrochem. Sci. Adv.*, 2022, **2**, e2100142.

37 H. Oswin and M. Salomon, *Can. J. Chem.*, 1963, **41**, 1686–1694.

38 H. Gerischer and A. Mauerer, *J. Electroanal. Chem. Interfacial Electrochem.*, 1970, **25**, 421–433.

39 R. M. Choueiri and L. D. Chen, *J. Phys. Chem. C*, 2022, **126**, 17952–17965.

40 M. U. Alzueta, V. D. Mercader, J. Gimenez-Lopez and R. Bilbao, *Fuel*, 2023, **353**, 129212.

41 H. Szichman, M. Baer, H.-R. Volpp and J. Wolfrum, *Symp. (Int.) Combust.*, 1998, **27**, 253–259.

42 H. Shin, S. Jung, S. Bae, W. Lee and H. Kim, *Environ. Sci. Technol.*, 2014, **48**, 12768–12774.

43 J. D. Gonzalez, K. Shojaee, B. S. Haynes and A. Montoya, *Phys. Chem. Chem. Phys.*, 2018, **20**, 25314–25323.

44 S. Garcia-Segura, M. Lanzarini-Lopes, K. Hristovski and P. Westerhoff, *Appl. Catal., B*, 2018, **236**, 546–568.

45 J. A. Dean, *Lange's Handbook of Chemistry*, McGraw-Hill, Inc., 1999.

46 R. Urrego-Ortiz, S. Builes, F. Illas and F. Calle-Vallejo, *EES Catal.*, 2024, **2**, 157–179.

47 R. Urrego-Ortiz, S. Builes and F. Calle-Vallejo, *Ind. Eng. Chem. Res.*, 2022, **61**, 13375–13382.

48 R. Urrego-Ortiz, S. Builes and F. Calle-Vallejo, *ChemCatChem*, 2021, **13**, 2508–2516.

49 L.-F. Huang, M. J. Hutchison, R. J. J. Santucci, J. R. Scully and J. M. Rondinelli, *J. Phys. Chem. C*, 2017, **121**, 9782–9789.

50 G. Kresse and J. Hafner, *Phys. Rev. B: Condens. Matter Mater. Phys.*, 1993, **47**, 558–561.

51 G. Kresse and J. Furthmüller, *Comput. Mater. Sci.*, 1996, **6**, 15–50.

52 G. Kresse and J. Furthmüller, *Phys. Rev. B: Condens. Matter Mater. Phys.*, 1996, **54**, 11169–11186.

53 A. Hjorth Larsen, J. Jørgen Mortensen, J. Blomqvist, I. E. Castelli, R. Christensen, M. Dułak, J. Friis, M. N. Groves, B. Hammer, C. Hargus, E. D. Hermes, P. C. Jennings, P. Bjerre Jensen, J. Kermode, J. R. Kitchin, E. Leonhard Kolsbjerg, J. Kubal, K. Kaasbjerg, S. Lysgaard, J. Bergmann Maronsson, T. Maxson, T. Olsen, L. Pastewka, A. Peterson, C. Rostgaard, J. Schiøtz, O. Schütt, M. Strange, K. S. Thygesen, T. Vegge, L. Vilhelmsen, M. Walter, Z. Zeng and K. W. Jacobsen, *J. Phys.: Condens. Matter*, 2017, **29**, 273002.

54 B. Hammer, L. B. Hansen and J. K. Nørskov, *Phys. Rev. B: Condens. Matter Mater. Phys.*, 1999, **59**, 7413.

55 P. E. Blöchl, *Phys. Rev. B: Condens. Matter Mater. Phys.*, 1994, **50**, 17953–17979.

56 G. Kresse and D. Joubert, *Phys. Rev. B: Condens. Matter Mater. Phys.*, 1999, **59**, 1758–1775.

57 Z. Szotek, W. M. Temmerman and H. Winter, *Phys. Rev. B: Condens. Matter Mater. Phys.*, 1993, **47**, 4029–4032.

58 J. A. Majewski and P. Vogl, *Phys. Rev. B: Condens. Matter Mater. Phys.*, 1992, **46**, 12219–12234.

59 A. Rohrbach, J. Hafner and G. Kresse, *Phys. Rev. B: Condens. Matter Mater. Phys.*, 2004, **69**, 075413.

60 A. Rohrbach and J. Hafner, *Phys. Rev. B: Condens. Matter Mater. Phys.*, 2005, **71**, 045405.

61 A. M. Ferrari, C. Pisani, F. Cinquini, L. Giordano and G. Pacchioni, *J. Chem. Phys.*, 2007, **127**, 17.

62 Y. Yuan, X. Dong and L. Ricardez-Sandoval, *Appl. Surf. Sci.*, 2019, **498**, 143782.

63 F. Cinquini, L. Giordano and G. Pacchioni, *Theor. Chem. Acc.*, 2008, **120**, 575–582.

64 H. Kedesdy and A. Drukalsky, *J. Am. Chem. Soc.*, 1954, **76**, 5941–5946.

65 A. Jain, S. P. Ong, G. Hautier, W. Chen, W. D. Richards, S. Dacek, S. Cholia, D. Gunter, D. Skinner, G. Ceder and K. A. Persson, *APL Mater.*, 2013, **1**, 011002.

66 H. J. Monkhorst and J. D. Pack, *Phys. Rev. B*, 1976, **13**, 5188–5192.

67 J. K. Nørskov, J. Rossmeisl, A. Logadottir, L. Lindqvist, J. R. Kitchin, T. Bligaard and H. Jónsson, *J. Phys. Chem. B*, 2004, **108**, 17886–17892.

68 L. D. Chen, J. K. Nørskov and A. C. Luntz, *J. Phys. Chem. Lett.*, 2015, **6**, 175–179.

69 R. A. Van Santen, M. Neurock and S. G. Shetty, *Chem. Rev.*, 2009, **110**, 2005–2048.

70 J. Cheng, P. Hu, P. Ellis, S. French, G. Kelly and C. M. Lok, *J. Phys. Chem. C*, 2008, **112**, 1308–1311.

71 P. Patil and L. Kadam, *Appl. Surf. Sci.*, 2002, **199**, 211–221.

72 I. Hotovy, J. Huran and L. Spiess, *J. Mater. Sci.*, 2004, **39**, 2609–2612.

73 W. Roth, *Phys. Rev.*, 1958, **110**, 1333.

74 A. Cheetham and D. Hope, *Phys. Rev. B: Condens. Matter Mater. Phys.*, 1983, **27**, 6964.

75 G. Sawatzky and J. Allen, *Phys. Rev. Lett.*, 1984, **53**, 2339.

76 E. Platero, B. Fubini and A. Zecchina, *Surf. Sci.*, 1987, **179**, 404–424.

77 N. Yu, W.-B. Zhang, N. Wang, Y.-F. Wang and B.-Y. Tang, *J. Phys. Chem. C*, 2008, **112**, 452–457.

78 B. Wang, J. Nisar and R. Ahuja, *ACS Appl. Mater. Interfaces*, 2012, **4**, 5691–5697.

79 J. Xiang, B. Xiang and X. Cui, *New J. Chem.*, 2018, **42**, 10791–10797.

80 K. Zhu, F. Shi, X. Zhu and W. Yang, *Nano energy*, 2020, **73**, 104761.

81 A. Ruiz Puigdollers, P. Schlexer, S. Tosoni and G. Pacchioni, *ACS Catal.*, 2017, **7**, 6493–6513.

82 G. He, M. Gao, Y. Peng, Y. Yu, W. Shan and H. He, *Environ. Sci. Technol.*, 2021, **55**, 6995–7003.

83 C. Lin, Y. Zhao, H. Zhang, S. Xie, Y.-F. Li, X. Li, Z. Jiang and Z.-P. Liu, *Chem. Sci.*, 2018, **9**, 6803–6812.

84 S. Chen, J. Xu, J. Chen, J. Li, Y. Yao, Z. Wang and F. Wang, *J. Alloys Compd.*, 2024, **1003**, 175650.